

Gnani, F., Zare-Behtash, H., White, C. and Kontis, K. (2018) Effect of back-pressure forcing on shock train structures in rectangular channels. *Acta Astronautica*, 145, pp. 471-481. (doi:[10.1016/j.actaastro.2018.02.010](https://doi.org/10.1016/j.actaastro.2018.02.010))

This is the author's final accepted version.

There may be differences between this version and the published version. You are advised to consult the publisher's version if you wish to cite from it.

<http://eprints.gla.ac.uk/157358/>

Deposited on: 16 February 2018

Effect of Back-pressure Forcing on Shock Train Structures in Rectangular Channels

F. Gnani,^{*} H. Zare-Behtash, C. White, and K. Kontis

University of Glasgow, School of Engineering, Glasgow G12 8QQ, UK

Abstract

The deceleration of a supersonic flow to the subsonic regime inside a high-speed engine occurs through a series of shock waves, known as a shock train. The generation of such a flow structure is due to the interaction between the shock waves and the boundary layer inside a long and narrow duct. The understanding of the physics governing the shock train is vital for the improvement of the design of high-speed engines and the development of flow control strategies. The present paper analyses the sensitivity of the shock train configuration to a back-pressure variation. The complex characteristics of the shock train at an inflow Mach number $M=2$ in a channel of constant height are investigated with two-dimensional RANS equations closed by the Wilcox $k-\omega$ turbulence model. Under a sinusoidal back-pressure variation, the simulated results indicate that the shock train executes a motion around its mean position that deviates from a perfect sinusoidal profile with variation in oscillation amplitude, frequency, and whether the pressure is first increased or decreased.

^{*} f.gnani.1@research.gla.ac.uk

I. NOMENCLATURE

C_P	Specific heat of air at constant pressure [J/kgK]
D_{eq}	Equivalent duct diameter [m]
e	specific internal energy
f	Frequency [Hz]
H	Test section height [m]
h	Specific enthalpy [J/kg]
k	Turbulence kinetic energy per unit mass [m^2/s^2]
L	Test section length [m]
M	Mach number
P	Pressure [Pa]
Pr	Prandtl number
q	Heat flux
R_S	Ratio of accumulation of error
S	Mean strain-rate tensor
T	Temperature [K]
t	Time [s]
U	Vector of velocity [m/s]
u	Component i of the velocity vector [m/s]
W	Test section width [m]
x	Component i of the position vector [m]
α	Closure coefficients
β	Closure coefficients
δ	Boundary layer thickness [mm]
δ_{ij}	Kronecker delta
ε	Back-pressure amplitude coefficient
ω	Radian frequency
σ	Closure coefficients
τ	Viscous stress tensors

Subscript

b	Back-pressure
i	Index of matrix element
j	Index of vector element
0	Total condition

Superscript

$*$	Steady condition
$+$	Maximum value
$-$	Minimum value

II. INTRODUCTION

The study of air-breathing intakes is vital for future space transportation and hypersonic flight applications. Since these intakes have no moving parts, the flow compression is achieved by means of a shock wave structure called a shock train. The characteristics of such a shock system depend on a number of variables including: the passage geometry, wall friction, Mach number, Reynolds number based on the duct hydraulic diameter, boundary layer thickness, and pressure conditions at the two extremities of the duct.¹⁻⁶ It has been reported that the shock wave structure changes depending mainly on the variation of the boundary layer thickness upstream of the shock train.⁷⁻⁹ This is in agreement with Babinsky & Harvey,¹⁰ who reported that multiple shocks are more likely to occur when the ratio of boundary layer displacement thickness to duct height is greater than a few percent.

The shock wave/boundary layer interaction that takes place in internal flows with inflow Mach numbers greater than 1.5 is characterised by an initial normal shock wave in the centre of the duct.¹¹ This shock wave splits into an oblique shock as it interacts with the boundary layer near the wall forming the so-called normal shock train configuration, as illustrated in Figure 1. The thick boundary layer and the shock pressure rise generate locally separated regions with the formation of a throat-like shape between two subsequent shocks that results in a change in the effective duct cross section. Therefore, immediately downstream

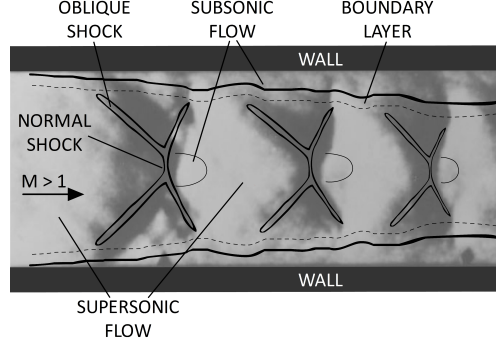


Figure 1. Shock wave/boundary layer interaction.¹²

of the leading shock wave, the flow is reaccelerated to supersonic speeds through a virtual nozzle until the occurrence of the next shock.¹³ The process of sequential decelerations and accelerations of the flow continues up to the point where a terminal shock occurs and the flow remains subsonic in the remaining part of the duct.¹⁴

As the Mach number increases, the flow pattern changes shape due to the stronger interaction with the boundary layer. The transition takes place for a Mach number in the range between 2 and 3, but depends also on the presence of fuel injection.^{15,16} All the shock waves composing the shock train assume an inclined configuration, leading to a flow pattern called an oblique shock train.¹⁷

The numerous variables which contribute to generating a complicated interaction between the shocks and the boundary layer make a comprehensive analysis of the flow field extremely difficult. Understanding the flow physics in the presence of the interaction of multiple shock waves with the boundary layer in internal flows is particularly challenging but essential to develop methods to predict and control the shock train. Analytical models are capable of outlining the general behaviour of the pressure rise through the shock train, however, such solutions rarely match experimental data. Another approach to study the shock trains is by numerically solving the compressible Navier-Stokes (NS) equations. Computational fluid dynamics (CFD) enables a detailed analysis of the flow field but few satisfactory results have been found in literature.

The choice of the turbulence model that closes the NS equations depends on the flow regime under investigation and is guided by the need for an accurate solution which can be achieved in a reasonable timescale.¹⁸ By using the Reynolds stress transport models (RSM)

Mousavi et al.¹⁹ successfully predicted the position and the shape of the shock train in a convergent-divergent nozzle. The employment of the shear stress transport model (SST) allowed Saha et al.²⁰ to achieve a good agreement between the predicted and measured wall pressure in an intake with freestream Mach number from 3 to 8. Zhang et al.²¹ found the SST model suitable to solve the flow field in isolators with adverse pressure gradients caused by the combustion heat release. Conversely, the numerical simulation performed by Gawehn¹³ with the SST strongly deviated from experimental data.

Sun et al.²² claimed to have obtained good agreement with the experimental data using the algebraic Baldwin-Lomax turbulence model. However, the experimental data were satisfactorily replicated only in one case. The Boussinesq approximation that is implicit in the algebraic model limits an accurate description of separated flows.²³ The use of such a closure model gives satisfactory results in the absence of flow separation.²⁴ Knight²⁵ reported that the Baldwin-Lomax model does not precisely predict the recovery of a turbulent boundary layer downstream of a strong two-dimensional shock interaction. Carroll et al.²⁶ compared the experimental data of a Mach 1.6 shock train in a rectangular duct and the RANS equations closed with the Baldwin-Lomax and the $k-\omega$ Wilcox-Rubesin models. As Figure 2 shows, both models fail to provide an accurate replication of the shock train. The

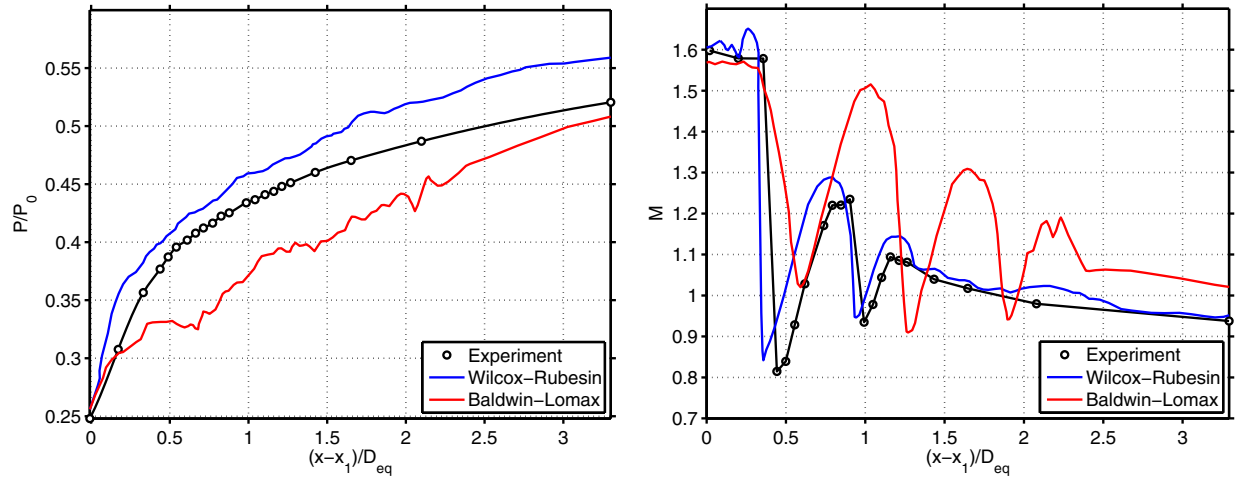


Figure 2. Wall static pressure (left) and centreline Mach number distribution (right), shifted for common pressure rise and normalised to the equivalent hydraulic diameter.²⁶

Baldwin-Lomax model is not capable of capturing the general features of the shock trains. The results obtained with the Wilcox-Rubesin model exhibits a more rapid pressure rise

compared to the Baldwin-Lomax model and better agrees with the Mach number profile. However, the pressure at the exit plane in the Wilcox-Rubesin model does not match the experimental value. The back-pressure was above the value experimentally observed in order to stabilise the shock train in the duct.

Compared to other turbulence models, the k - ω model seems to be the most appropriate choice to model shock trains. This model is able to reproduce subtle features close to the solid boundary and is more accurate for two-dimensional boundary layers with both favourable and adverse pressure gradients, and in the presence of separation induced by the interaction with a shock wave.²⁷ The details of a normal shock wave interacting with the boundary layer were well predicted in the case of attached boundary layer but, when flow separation is present, the discrepancies of the simulated results with experiments increased as separation becomes larger.²⁸ On the other hand, Chan et al.²⁹ more recently demonstrated that the Wilcox k - ω model is suitable for supersonic and hypersonic aerothermodynamic applications.

The objective of the present study is to first numerically replicate the experimental data collected by Sun et al.²² in a square duct with a Mach 2 shock train with two-dimensional RANS equations closed by the Wilcox k - ω turbulence model and then explore the response of the shock train under a periodical back-pressure forcing. Although the experimental flow physics is three-dimensional due to the effect of sidewalls, at the centre of the duct the flow can be assumed two-dimensional. The boundary layer affects the flow in proximity of the wall but in the centre of the duct the flow can be simulated with a two-dimensional code. As successfully demonstrated by Sun et al.,²² the effect of the sidewalls would not change the structure of the shock train in the centre of the duct. Such a simplification is not completely accurate but necessary to balance accuracy with computational resources.

III. NUMERICAL METHOD AND PHYSICAL SETUP

A. Numerical code

To validate the numerical approach, the Mach 2 shock train experimentally studied by Sun et al.^{22,30} in a square duct was initially replicated. The boundary and geometrical conditions are reported in Table I.

The numerical simulations were carried out solving two-dimensional coupled implicit

M	$T_0[K]$	$P_0[kPa]$	$P_b[kPa]$	$H[mm]$	$W[mm]$	$L[mm]$	δ/D_{eq}
2	300	196	92.2	80	80	880	0.25

Table I. Boundary and geometry conditions of the computational domain of the validation model.²² The subscript 0 refers to the total condition and P_b is the back-pressure.

Reynolds-averaged Navier-Stokes (RANS) equations, in Equations 1 to 3, in STAR-CCM+³¹ with the Wilcox k - ω turbulence model, in Equations 7 and 8.

$$\frac{\partial \rho}{\partial t} + \frac{\partial}{\partial x_j} (\rho U_j) = 0 \quad (1)$$

$$\frac{\partial}{\partial t} (\rho U_i) + \frac{\partial}{\partial x_j} (\rho U_i U_j) = -\frac{\partial P}{\partial x_i} + \frac{\partial \tau_{ji}}{\partial x_j} \quad (2)$$

$$\frac{\partial}{\partial t} \left[\rho \left(e + \frac{1}{2} U_i U_i \right) \right] + \frac{\partial}{\partial x_j} \left[\rho U_j \left(h + \frac{1}{2} U_i U_i \right) \right] = \frac{\partial}{\partial x_j} (U_i \tau_{ij}) - \frac{\partial q_j}{\partial x_j} \quad (3)$$

The symbols U_j and x_j are the j -th component of the velocity and position vectors, e is the specific internal energy, $h = e + P/\rho$ is the specific enthalpy, t is the time, P is the pressure, ρ is the density, q_j is the heat flux, and τ_{ji} is the viscous stress tensors defined as:

$$\tau_{ij} = 2\mu S_{ij} \quad (4)$$

The mean strain-rate tensor, S_{ij} , is specified as follows:

$$S_{ij} = \frac{1}{2} \left(\frac{\partial U_i}{\partial x_j} + \frac{\partial U_j}{\partial x_i} \right) - \frac{1}{3} \frac{\partial U_k}{\partial x_k} \delta_{ij} \quad (5)$$

where δ_{ij} is the Kronecker delta. The heat flux, q_j , is defined by Equation 6 in which λ is the thermal conductivity and Pr is the laminar Prandtl number.

$$q_j = -\lambda \frac{\partial T}{\partial x_j} = -C_P \frac{\mu}{Pr} \frac{\partial T}{\partial x_j} \quad (6)$$

The Prandtl number depends on the properties of the fluid only, and is governed by the ratio of the dynamic viscosity and heat conductivity, therefore $Pr = 1$ implies a perfect balance between viscous dissipation and heat conduction, and hence the wall is adiabatic.³²

$$\frac{\partial}{\partial t} (\rho k) + \frac{\partial}{\partial x_j} (\rho U_j k) = \frac{\partial}{\partial x_j} \left[(\mu + \sigma_k \mu_t) \frac{\partial k}{\partial x_j} \right] + \rho \tau_{ij} \frac{\partial U_i}{\partial x_j} - \beta^* \rho \omega k \quad (7)$$

$$\frac{\partial}{\partial t}(\rho\omega) + \frac{\partial}{\partial x_j}(\rho U_j \omega) = \frac{\partial}{\partial x_j} \left[(\mu + \sigma_\omega \mu_t) \frac{\partial \omega}{\partial x_j} \right] + \alpha \frac{\omega}{k} \rho \tau_{ij} \frac{\partial U_i}{\partial x_j} - \beta \rho \omega^2 + \sigma_d \frac{\rho}{\omega} \frac{\partial k}{\partial x_j} \frac{\partial \omega}{\partial x_j} \quad (8)$$

The RANS equations are discretised using the cell-centred finite volume method. The inviscid and viscous fluxes are evaluated using respectively the Liou's AUSM+ flux-vector splitting scheme based on the upwind concept and the second-order central differences. The temporal term is discretised with a second-order accuracy interpolation scheme.

B. Physical setup

The working fluid is approximated as an ideal gas.^{3,19} The viscosity and thermal conductivity are evaluated using Sutherland's law. Adiabatic and no-slip boundary conditions are imposed on the walls along the channel. Initial conditions are set with an inviscid normal shock at the exit of the computational domain. Stagnation conditions are imposed at the inlet with uniform flow properties. At the outlet boundary the flow variables except pressure are extrapolated from the adjacent cell value using reconstruction gradients. The back-pressure was determined from the experimental results to be approximately $P_b = 92.2$ kPa and assumed constant at the exit plane.

The computational domain is formed by a channel of constant height equal to 80 mm. The effect of the flow confinement, δ/D_{eq} , at the inlet of the computational domain plays a fundamental role in the location of the shock train. In this study a computational domain with $L/D_{eq} = 23$ has been used because the boundary layer requires an additional length of the channel ahead of the shock train to fully establish. This value has been chosen after an iterative process of mesh refinement and channel length analysis. Only the portion of channel with length 11 times the height was taken to process the data, with the inlet located at δ/D_{eq} equal to approximately 0.25.²²

Due to the symmetry of the problem to the channel centreline only half of the flow field is computed. The grid is composed of structured quadrilateral cells that are clustered towards the wall to resolve the behaviour of the boundary layer. Figure 3 shows the structure of the numerical grid employed, where $y/D_{eq} = 0$ corresponds to the wall and $y/D_{eq} = 0.5$ is the centreline of the channel.

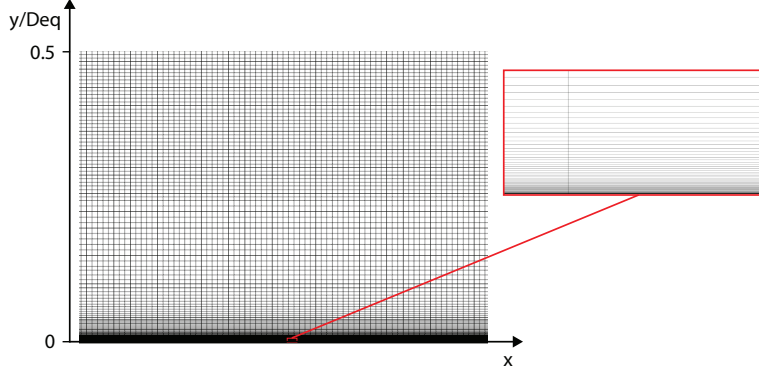


Figure 3. Portion of the half duct numerical grid employed in the 2D computational domain.

C. Grid independence

The quality of the solution depends on a number of variables, but mainly on the size of the grid cells and their distribution in the computational domain. While few cells may cause poor results because important flow characteristics are not resolved, in most cases complete grid independence would lead to such a high number of cells that the achieved accuracy is not justified by the increased computational cost. Seven grids, tabulated in Table II, are employed to find the optimal combination between the requirements of adequate accuracy and computational resources. Except for Grid 1, with all the finer grids the value of wall

Grid	1	2	3	4	5	6	7
N_x	368	921	2454	4601	6134	9200	12268
N_y	62	116	154	276	314	350	452

Table II. Number of cells in different grids.

y^+ is smaller than unity in the entire domain, providing a good resolution of the boundary layer gradients.

Static pressure with different grid sizes are compared in Figure 4. The wall static pressure, in Figure 4(a), monotonically increases due to the diffusing effect of the boundary layer. The pressure profiles illustrate the relative difference in the location of the shock train in the channel with respect to the finest mesh. Figure 4(b) shows the pressure distribution at the channel centreline shifted by the location of the initial shock wave. The pressure undergoes a series of peaks and troughs along the channel which represent the several shock

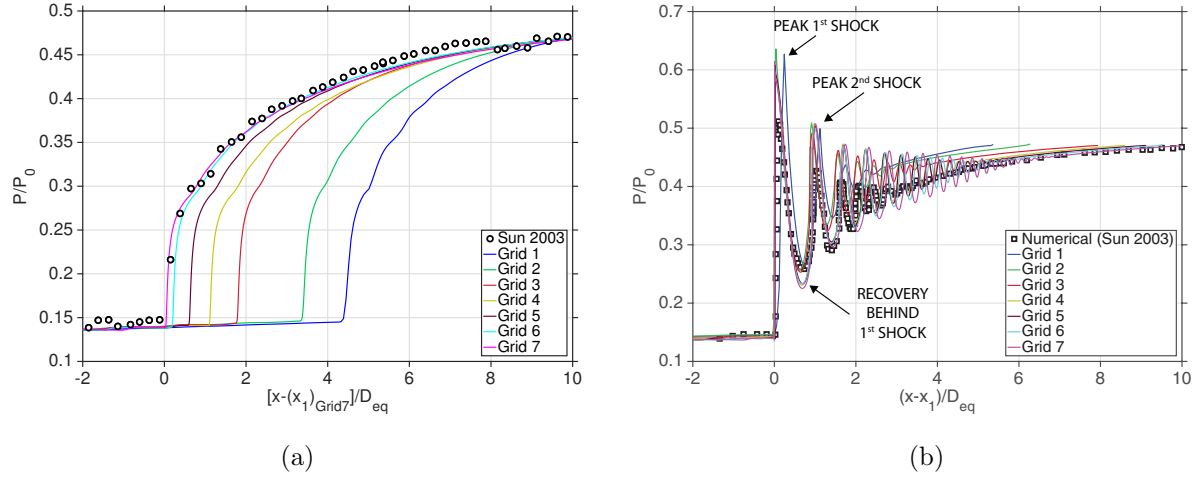


Figure 4. Effect of grid resolution on pressure. a) Wall pressure; b) Centreline pressure.

waves composing the shock train which are gradually damped along the channel.

The numerical pressure contour obtained with the various grids, in Figure 5, shows that the general behaviour of the shock train is similar in the seven cases. However, a very coarse

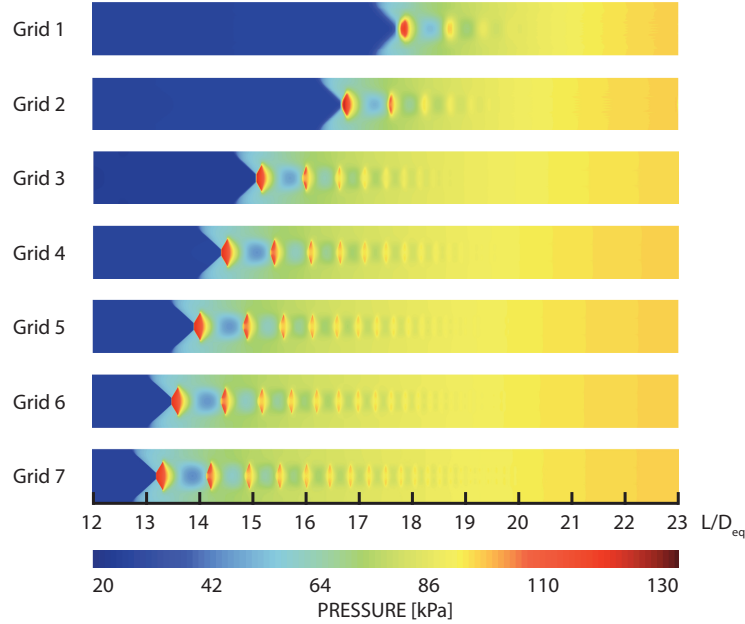


Figure 5. Numerical contours of pressure with different grid resolution.

mesh fails to adequately resolve fine structures such as the boundary layer. Fine grids better match the experimental data because the representation of the flow field is more accurate. In such flows, where the ratio of the thickness of the boundary layer to the channel height is a

key parameter in determining the shock train characteristics, an error of only a few percent in resolving the boundary layer can result in a considerable divergence from the experiments. Since the back-pressure is prescribed as a boundary condition, the pressure at the end of the shock train tends towards the experimental value. As the grid resolution increases, the shock train moves upstream towards the inlet and increases in length. These results agree with most cases in the literature, although Carroll et al.²⁶ found that the shock train moves towards the exit plane as the grid is refined in the transverse direction. Nevertheless, as the grid is refined, the difference between two subsequent pressure profiles gradually decreases and the location of the shock train tends to stabilise at a fixed axial coordinate, as illustrated in Figure 6(a). The difference between Grid 6 and Grid 7 is not significant and the relative

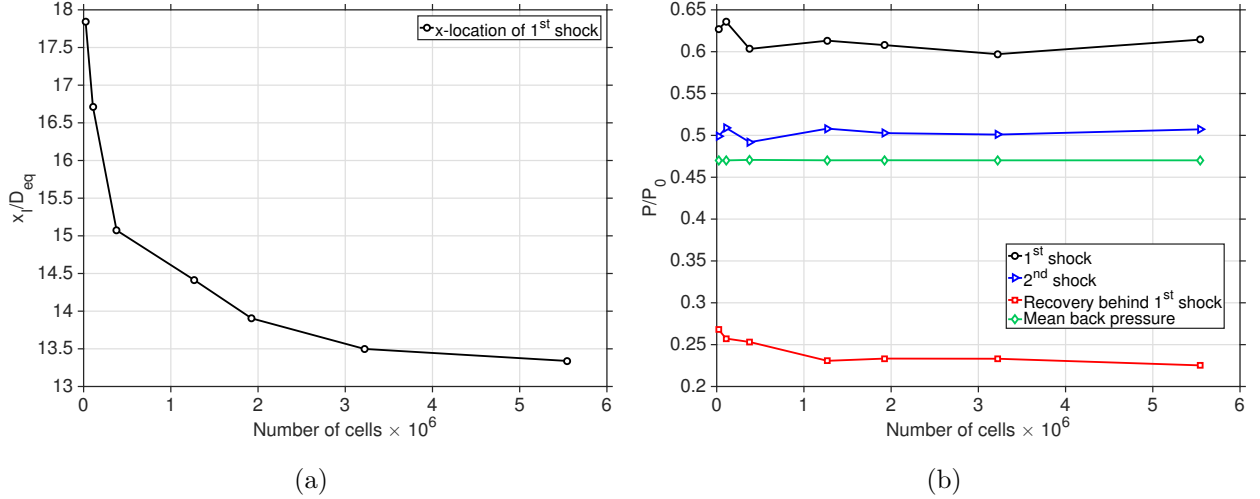


Figure 6. Variation with grid resolution of: a) Axial coordinate of the leading shock wave; b) Value of pressure in different parts of the shock train.

error is less than 1.2%.

The magnitude of the pressure peaks of the first and second shocks from Figure 4(b), respectively peak 1st shock and peak 2nd shock, as well as the pressure recovery behind the 1st shock are reported in Figure 6(b). From Grid 4 to Grid 7 the variation in magnitude of the first and second shock is very small, respectively 0.20% and 0.17%, as it is evident also from the pressure profiles in Figure 4(b). Taking into account both the accuracy of the grid with the computational cost, Grid 6 is used to perform the simulations reported in this work unless otherwise specified.

IV. RESULTS AND DISCUSSION

A. Steady flow

The presence of the flow confinement at the inlet of the computational domain due to viscous effects plays a fundamental role on the location of the shock train. In internal supersonic flows, in response to the presence of a downstream pressure rise, the flow interacts with the boundary layer forming a shock train, schematically illustrated in Figure 7. The

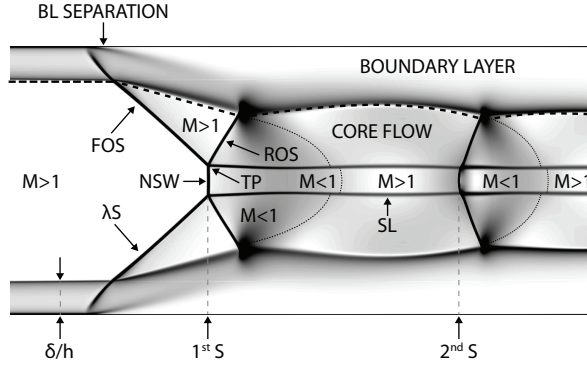


Figure 7. Schematic of the shock wave/boundary layer interaction in shock train.

flow enters the inlet at supersonic speeds and is decelerated to subsonic velocity behind the first normal shock wave, *NSW*, in the core flow. The pressure rise is transmitted upstream through the boundary layer region, causing a thickening of the boundary layer itself. The growth of the boundary layer deflects the streamline forming an oblique shock, *FOS*. Since the flow remains supersonic behind the front oblique shock, a rear oblique shock wave, *ROS*, forms behind it. The two oblique shocks converge into the triple point, *TP*, and combine with the initial normal shock into a λ shock structure, λS . At the point of bifurcation, a shear layer, *SL*, develops, as can be observed in the form of slip lines. In the region confined between the slip lines, the stronger deceleration through the normal shock produces a misalignment with the outer parts where the flow passes through the two oblique shocks.

The thickening of the boundary layer reduces the effective area of the core flow, so that the subsonic flow behind the rear oblique shock wave, *ROS*, is accelerated again to supersonic velocity. At this point the supersonic flow interacts with the thick boundary layer and the same process is repeated few times up to a terminal shock after which the flow is subsonic

in the entire cross section.

B. Shock train characteristics with a periodic back-pressure

The response of the shock train to a change in the back-pressure is analysed with unsteady simulations. The steady state solution gives an averaged position of the shock train in the channel. However, in real supersonic air-breathing engines, the shock train behaviour is inherently unsteady and the entire structure is subject to fluctuations due to the longitudinal combustion instabilities.³³

The coupling between the shock train motion with the pressure fluctuations may generate noise or fluctuated wall loads.³⁴ Turbulent combustion in the combustion chamber is characterised by a stochastic character, which give birth to stochastic oscillations of parameters. However, as the pressure fluctuations produced in the combustor propagate upstream, interactions with the shock waves in the channel generate additional disturbances. These include self-sustained oscillations, shock-induced flow separation, and the influence of the first shock oscillation on the subsequent shocks.^{35–37} The latter phenomenon leads to the interaction of two oscillation frequencies which travel in the opposite direction and excite each other. The acoustic waves, when interacting with the shock waves in the shock train, establish a periodic oscillation.³³ Another sources of periodic back pressure oscillations arise also from the pulse detonation combustion mode in the engine.

In the present study the acoustic motion induced by unsteady combustion is reproduced by means of sinusoidal pressure oscillations imposed at the exit plane with Equation 9.

$$P(t) = P^* [1 + \varepsilon \sin(\omega t)] \quad (9)$$

The variable P^* identifies the back-pressure applied in the steady case and the oscillation amplitude coefficient, ε , is varied between 0.01 and 0.1. These values are used to model different flow conditions subject to back-pressure changes in the combustion chamber of an air-breathing engine. In fact, if the back-pressure is too large the shock system is not able to compensate the pressure rise and propagates upstream until it is disgorged from the inlet.

1. Effect of numerical grid on the time step

The suitable time step is related to the dimensions of the grid cells, therefore the optimum time step changes for grids of different resolution.³⁸ As previously mentioned, except the coarser grid, Grid 1, no substantial differences are observed in the shape of the first shock wave. Since the strength of the first shock determines the structure of the entire shock train, the first shock wave is used as a reference to detect the axial movement of the shock train in the channel and the change in magnitude during a period of the back-pressure forcing. In this section the solutions using Grid 2, Grid 4, and Grid 6 are compared.

Four time steps are used based on the characteristic time, T_c , defined as L/u_∞ , where L is the length of the computational domain and u_∞ the freestream velocity. The time step size $\Delta T_1 = 0.1 T_c$ is used as baseline case and three further refinements were taken halving the previous time step, i.e. $\Delta T_2 = 0.05 T_c$, $\Delta T_3 = 0.025 T_c$, and $\Delta T_4 = 0.0125 T_c$. The effect of the time step on the numerical solution is investigated with a periodic wave of amplitude $\varepsilon = 0.1$ and frequency $f = 2 \text{ Hz}$. An amplitude of approximately 10% of the steady value is representative of the variation of the pressure in the combustion chamber of a ramjet with inflow Mach number of $M = 2$. The value of the frequency is chosen because this replicates similar flow conditions that can be established in an experimental facility at the University of Glasgow.

Figure 8(a) shows the time history of the movement of the leading shock in the axial direction with Grid 2, normalised by its values at the rest point before any downstream pressure forcing is imposed. After the first cycle, the oscillatory motion settles down and all remaining oscillations occur between the same minimum and maximum axial positions, x^- and x^+ , respectively. The collapsed curve in Figure 8(b) is obtained from four consecutive oscillation periods and shows that the solution is independent of the time step.

The relation between the grid dimension and the time step size is illustrated in Figure 9. Figure 9(a) shows that by increasing the grid size with the time step ΔT_1 , the displacement of the leading shock from its initial position decreases considerably. Moreover, by using Grid 6 the position of the leading shock during a back-pressure cycle does not reproduce the sinusoidal variation. On the other hand, by using a smaller time step, ΔT_2 in Figure 9(b) and ΔT_3 in Figure 9(c), the solution increases in accuracy and the variation in the position of the first shock during a period exhibits a sinusoidal behaviour with all the grids.

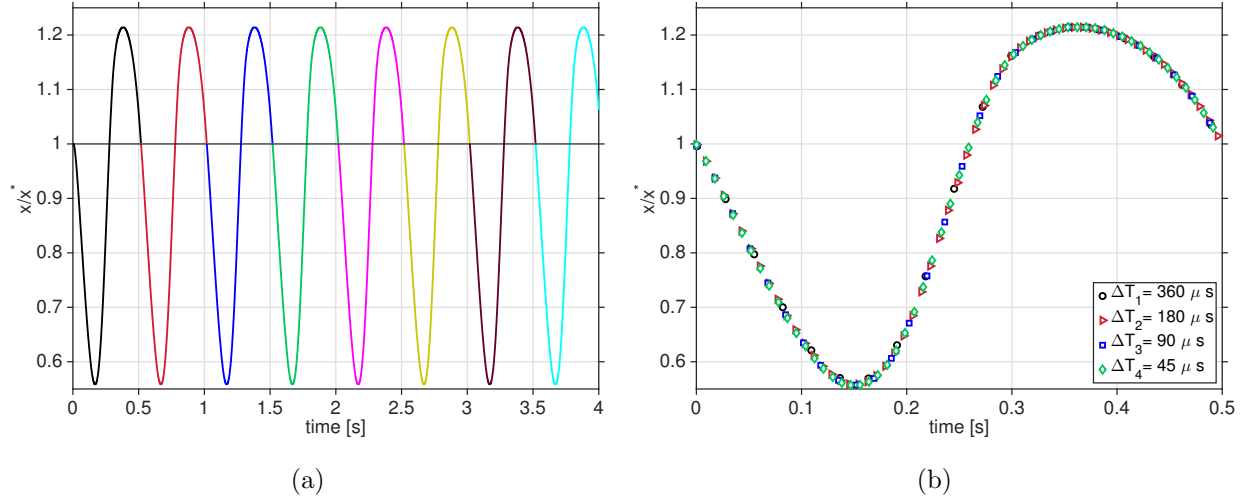
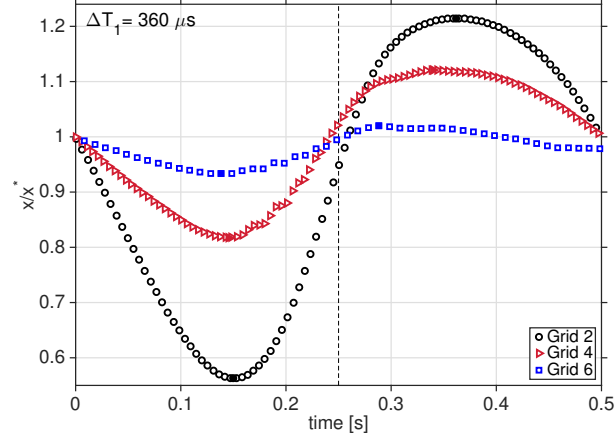


Figure 8. a) Time history of the normalised position of the leading shock in the axial direction with Grid 2 and ΔT_2 ; b) Collapsed curve of the normalised location of the leading shock in the axial direction with Grid 2 and different time steps.

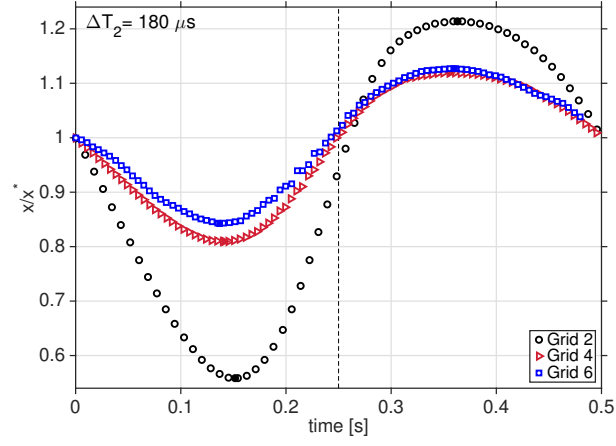
The difference in the displacement of the leading shock from its initial position obtained with Grid 4 and Grid 6 becomes gradually smaller. In particular, with ΔT_3 , the solution obtained with Grid 4 and Grid 6 overlap. Small discrepancies arise from the dependence of the solution on the grid size. The reason of the divergence of the oscillations obtained with Grid 2 is the large variations in the outlet velocity profile and boundary layer thickness that are not accurately resolved with a coarse mesh. As the number of cells increase, the flow field is replicated at a more detailed level. As a consequence, the time step confirms to be strongly related to the dimensions of the grid. The time step ΔT_1 is not adequate to resolve the flow with fine grids which require a smaller time step. For Grid 4 the time step ΔT_2 is adequate, but Grid 6 requires ΔT_3 .

In conclusion, from all the grids employed it emerges that the furthest upstream and downstream axial position reached by the shock train in the channel are different. The response of the shock train to a symmetrical variation in back-pressure is not symmetrical. An increase in the back-pressure always leads to a movement upstream towards the inlet of greater magnitude compared to the movement towards the outlet caused by a decrease in the back-pressure. The influence of a pressure increase compared to a pressure drop does not depend on neither the grid size nor the time step.

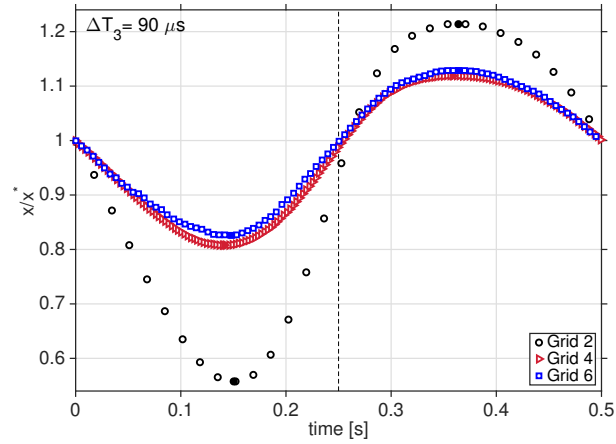
Simulations of complex unsteady flows are subject to the accumulation of errors that



(a)



(b)



(c)

Figure 9. Position of the leading shock in the axial direction with different grid size and time step.

a) ΔT_1 ; b) ΔT_2 ; c) ΔT_3 .

depend on the spatial resolution and the numerical solver. The errors from integration accumulate for successive time steps. Following the procedure outlined by Smirnov,³⁹ the accumulation of errors is determined estimating the relative error in the directions of integration in function of the cell size, the domain size, and the order of accuracy of the numerical scheme. The allowable value of total error, defined by the user to be in the range between 1% and 5%, allows to define the maximal allowable number of time steps for solving a problem. The ratio of the maximal allowable number of time steps for the problem and the actual number of time steps used to obtain the result, R_S , characterises the reliability of results. For high values of R_S the error is low, while the error tends to the maximal allowable value for R_S tending to unity. For the present study, with the time step ΔT_3 , R_S has been found equal to 7.03×10^2 , 5.52×10^6 , and 2.30×10^7 for Grid 2, Grid 4, and Grid 6, respectively. This illustrates that, in terms of accumulation of errors, the unsteady solutions with the three grids are reliable, and the accuracy increases as the grid is refined.

2. *Description of periodic oscillation*

Although Grid 2 provides a solution of limited accuracy, it is capable of outlining the general characteristics of the shock train oscillation but requires a considerably smaller amount of computational resources compared to the finer grids. Therefore, this grid is considered adequate to perform the analysis of the shock train in the presence of a back-pressure forcing.

Figure 10 shows that, despite the fact that the forcing imposed at the exit plane is symmetrical, the response of the shock train does not match the same trend of the back-pressure. During the cyclic motion, the shock train travels back and forth from its initial position, x^* . As the temporal evolution of the Mach number, in Figure 11, illustrates, to an increase in the back-pressure, the shock train responds by moving upstream towards the inlet of the computational domain. On the contrary, a decrease in the back-pressure forces the shock train to move towards the outlet. The distance covered by the shock train in the upstream portion of the channel is approximately double of that covered in the downstream portion, as illustrated in Figure 10. This means that the shock train moves faster upstream than downstream since the time to move in both directions is the same. The response of the shock train when subject to a periodic back-pressure variation shows the presence of

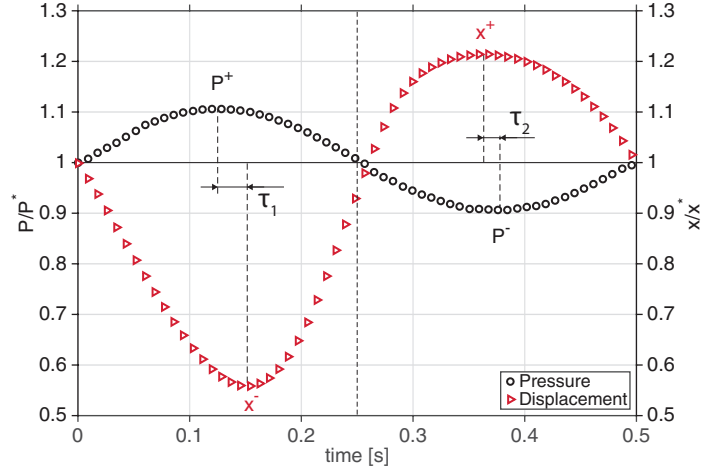


Figure 10. Plot of normalised forcing pressure and location variation of the leading shock with Grid 2 and ΔT_2 .

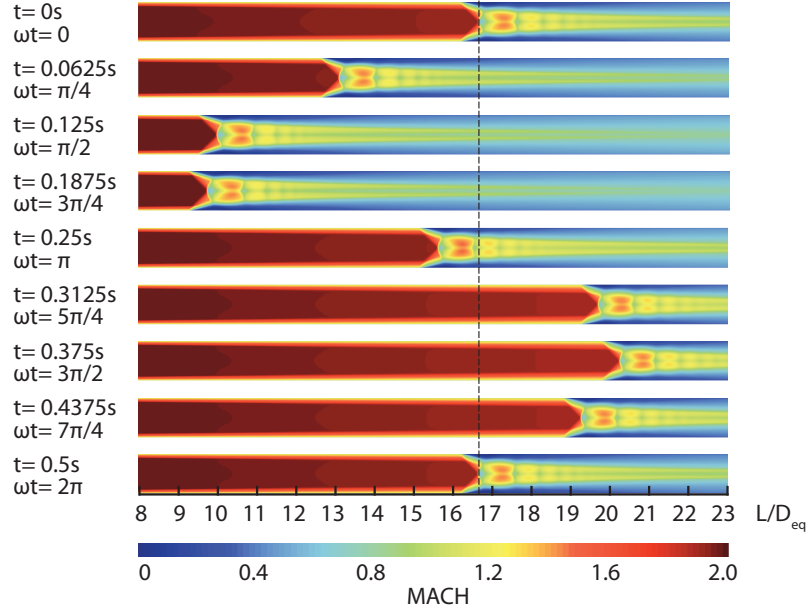


Figure 11. Temporal evolution of the computed Mach number contour with Grid 2 and time step ΔT_2 .

non-linear phenomena due to the interactions between the shock waves with the boundary layer. These effects, that have been numerically identified by Hsieh et al.,⁴⁰ play a key role in determining the time history of the shock train position along the channel. However, in contrast to the present study, Hsieh et al.⁴⁰ observed a change in the shock train configuration during a back-pressure cycle mainly due to the non-constant cross-sectional area of the duct.

Another interesting observation is that the extremes of the shock train position, x^- and x^+ , occur at different time instants compared with the corresponding extremes in the back-pressure, P^+ and P^- , respectively. As Figure 10 illustrates, when the back-pressure increases, the minimum shock train position occurs with a delay, τ_1 , after the maximum in the back-pressure. The delay of the minimum shock train position, x^- , from the maximum back-pressure value, P^+ , shows that the flow responds to an external change with a time delay. This result is in agreement with Xu et al.,⁴¹ who justified with inertia the movement of the shock train for a distance when the increasing back-pressure is stopped. More interestingly, the downstream position is reached before the minimum back-pressure of a time shift τ_2 , due to the presence of a thicker boundary layer downstream that greatly influences the entire shock train when it travels towards the outlet.

Figure 12 shows the Mach number behind the leading shock during a pressure cycle and the temporal evolution of the centreline Mach number obtained with Grid 2 and time step ΔT_2 . In Figure 12(a) the variation of the Mach number behind the first shock wave is

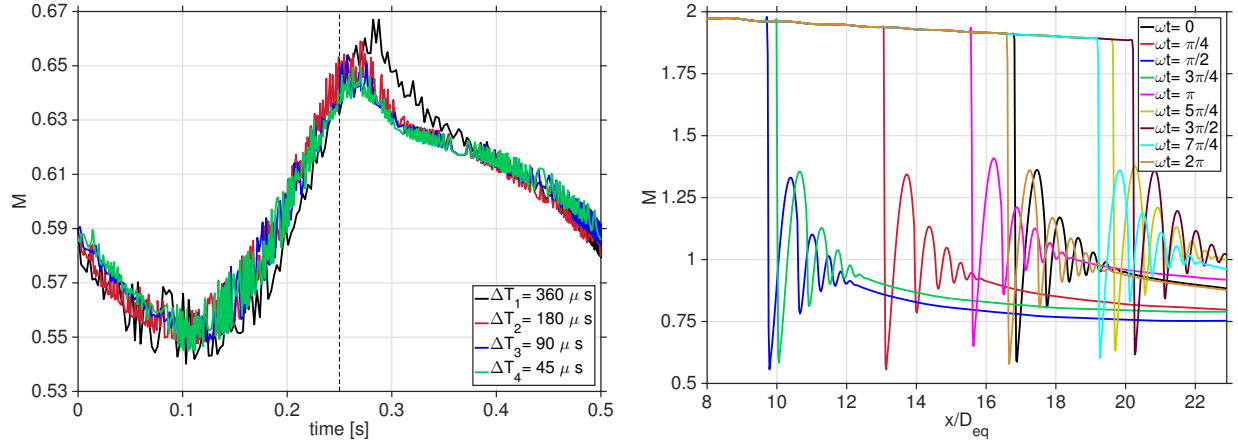


Figure 12. a) Time history of the Mach number behind the leading shock in the shock train during different cycles; b) Temporal evolution of the centreline Mach number.

characterised by a large oscillation due to the forcing and a small oscillation due to the unstable nature of the flow. With an increase in the back-pressure the shock train responds with a decrease in the flow speed meaning that the first shock is stronger and the flow is more strongly decelerated. On the contrary, when the back-pressure is decreased, the first shock becomes weaker and the flow speed increases. The variation of the Mach number in Figure 12(a) does not exhibit a sinusoidal variation. In the first half of the cycle, when

the back-pressure is increased, the variation of the Mach number exhibits a smooth wave behaviour. On the other hand, after the time instant $t = 0.25$ s, when the Mach number behind the leading shock reaches its maximum value, the second half of the cycle is no longer characterised by a sinusoidal wave. These changes are very small since in Figure 12(b) minimal variations are observed in the flow configuration, as also visible in the temporal evolution of the Mach number in Figure 11. Consequently, the back-pressure change of amplitude $\varepsilon = 0.1$ does not affect the shape of the shock train.

3. Effect of back-pressure variation

The asymmetric response of the leading shock position in the axial direction was further investigated applying the forcing pressure wave either with an initial pressure increase, $P(+)$, or a pressure decrease, $P(-)$. In Figure 13 $P(-)$ has been reversed in order to make the two plots comparable. Whether the pressure is first increased or decreased the time history of

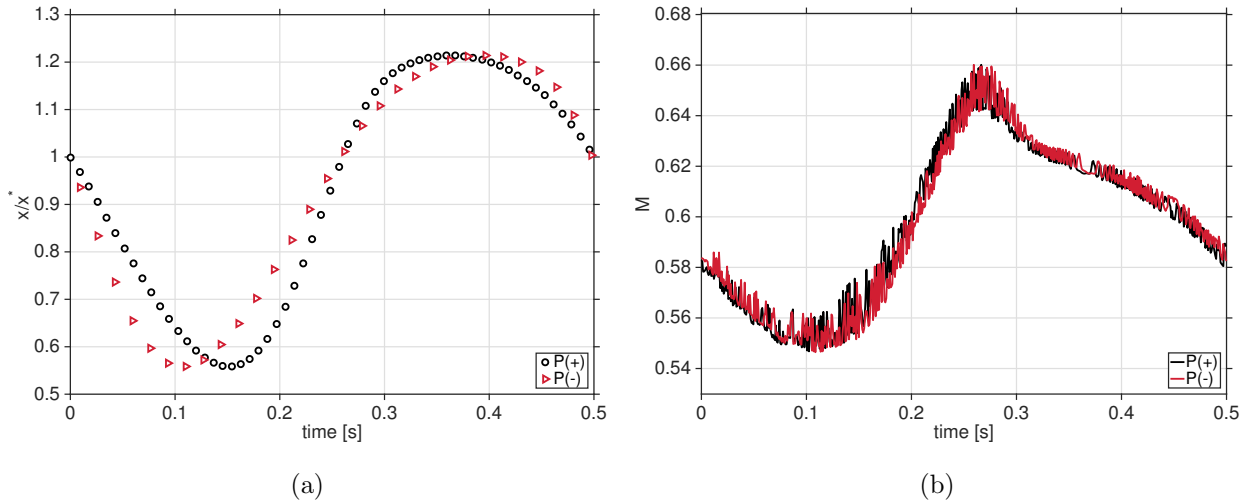


Figure 13. a) Position of the leading shock in the axial direction; b) Mach number behind the leading shock in the shock train.

the shock train position exhibits the same trend. Since the forcing has the same amplitude, the leading shock reaches the same minimum and maximum positions but the two paths do not completely overlap as Figure 13(a) illustrates. On the other hand, the Mach number, in Figure 13(b), shows that the strength of the leading shock varies with the same trend. This confirms that non-linear phenomena due to the interactions between the shock waves

with the boundary layer are present and play a key role in determining the time history of the shock train position along the channel. These effects, however, do not affect the change in the speed, consistently with the fact the velocity, and hence the Mach number, varies in the same way as the pressure, but with an altered phase angle.

4. Effect of forcing oscillation amplitude

The engine of a high-speed aircraft requires different combustion conditions during the various phases of the flight envelope. As a consequence, the flow structures which form at the inlet and inside the isolator are subject to transient conditions. The disturbances induced by changes in the combustion develop an oscillatory behaviour of the flow. Large oscillation amplitudes may cause the shock train to be expelled out of the inlet. Small oscillations of the order of a few percent of the mean pressure value characterise the dynamics of the combustion process in the engine.

In Figure 14 the effect of the oscillation amplitude with $\varepsilon = 0.01, 0.05$, and 0.1 are presented with an oscillation frequency $f = 2 \text{ Hz}$. With an oscillation amplitude of $\varepsilon = 0.2$

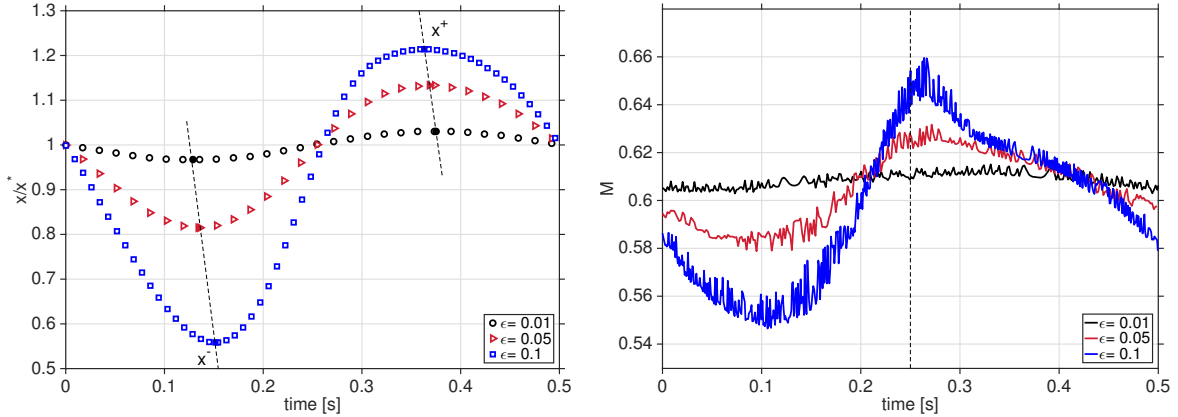


Figure 14. Effect of the oscillation amplitude: a) Position of the leading shock in the axial direction; b) Time history of the Mach number behind the leading shock in the shock train.

the shock train was disorged out of the inlet. In Figure 14(a), as the oscillation amplitude increases the difference between the maximum and minimum positions of the leading shock in the axial direction becomes more pronounced, in agreement with previous numerical studies.³³ While with small oscillation amplitudes, the ratio of the minimum to the maximum displacement, x^-/x^+ , is approximately unity, with increasing ε the displacement

of the minimum and maximum from the mean position, x^- and x^+ , proportionally increases. With $\varepsilon = 0.1$ the ratio of the minimum to the maximum displacement, x^-/x^+ , reaches the value of approximately 2.

Figure 14(a) illustrates that for each ε , x^- and x^+ are located along lines with negative slope. As ε increases, x^- is gradually delayed whereas x^+ occurs earlier in time. This means that, compared to a small oscillation amplitude, with a large oscillation amplitude the shock train covers a greater distance along the channel but takes more time to reach the furthest upstream axial position. After $t = 0.25$ s, when the back pressure is decreased, the shock train reaches the furthest downstream position earlier with increasing value of ε . This can be explained from the time history of the Mach number of the leading shock wave, in Figure 14(b). With a small value of ε , the leading shock responds with a small change in magnitude which is comparable to the oscillation inherent of the shock train unsteadiness. After the first quarter of the cycle, the back pressure starts to decrease from its maximum value with a gradient in the Mach number that is higher for large oscillation amplitudes, so that the shock train is subject to a greater acceleration. With a small oscillation amplitude the leading shock Mach number exhibits a less pronounced maximum value, and the time history of the response resembles more a sinusoidal wave. This suggests that the non-linear effects are enhanced as the wave amplitude increases but have a negligible influence when the back-pressure amplitude is small.

5. *Effect of forcing frequency*

Figure 15 shows the effect of different forcing frequencies, $f = 2$ Hz, 4 Hz, 10 Hz, 20 Hz, with the same oscillation amplitude. The x -axis is normalised to the period of the forcing wave. As Figure 15(a) illustrates, a decrease in the forcing frequency leads to a larger difference between x^- and x^+ , in agreement with what has been observed by previous studies.⁴² In the first half of the cycle, the minimum and maximum Mach number of the leading shock, M^- and M^+ in Figure 15(b), act in the opposite way compared to x^- and x^+ . As the forcing frequency increases, x^- tends to be delayed whereas M^- occurs earlier in time compared to low forcing frequencies. While for $f = 2$ Hz the minimum Mach number, M^- , occurs at approximately 1/4 of the x -axis, for $f = 20$ Hz the minimum Mach number is close to the mean value at the beginning of the period. A different behaviour is exhibited

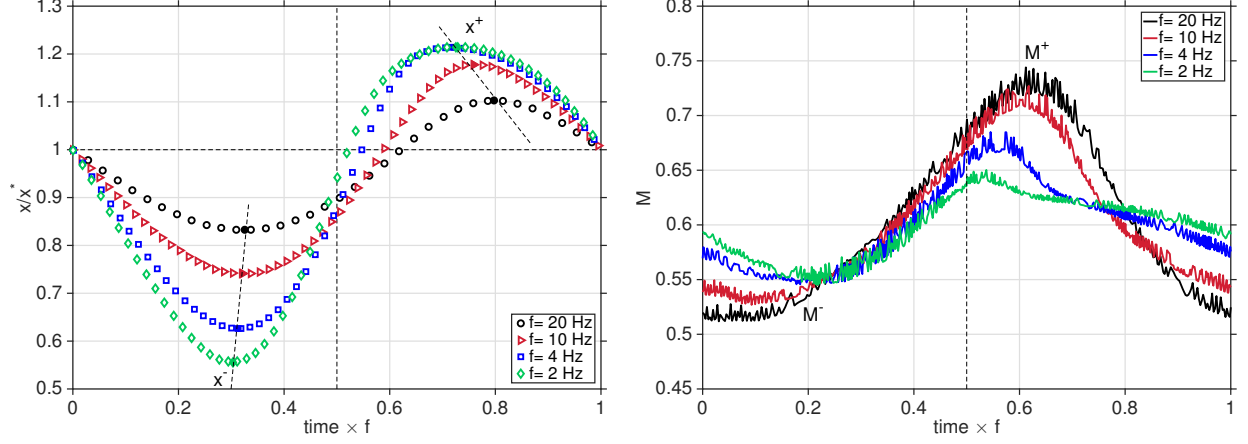


Figure 15. Effect of different forcing frequencies: a) Position of the leading shock in the axial direction; b) Mach number behind the leading shock in the shock train.

in the second part of the pressure cycle. Compared to low forcing frequencies, both x^+ and M^+ occur with an increasing time delay as the oscillating frequency assumes larger values. After the first half of the pressure cycle the shock train position does not recover to its initial value. Indeed, the shock train returns to its initial position with a greater delay as the forcing frequency increases.

It is interesting to note that the variation in the forcing frequency affects also the strength of the leading shock, in Figure 15(b). It is observed that for small frequencies the extremities of the Mach number profile are closer to the mean position. Additionally, the mean value itself changes, decreasing with higher frequencies. This may be caused by the establishment of additional mechanisms in the flow once a certain frequency is reached.

Therefore, high forcing frequencies reduce the axial movement of the leading shock but increase the range of Mach number values during a period. The interaction between the shock waves with the viscous effects introduce additional mechanisms in the flow that appear to be accentuated with higher frequencies in the oscillation of the back pressure. This is believed to be the reason of the change of the time instant when the leading shock returns to the initial location. The effect of the oscillation frequency and amplitude on the position of the leading shock is summarised in Figure 16. The non-linear phenomena are exhibited in the asymmetrical variation of the position of the leading shock with different oscillation frequency.

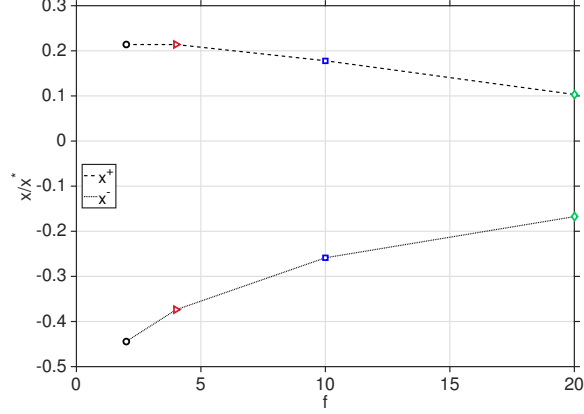


Figure 16. Effect of the oscillation frequency on the position of the leading shock with oscillation amplitude $\varepsilon = 0.1$.

V. CONCLUSIONS

The formation of a shock train structure in an air-breathing engine prevents the disturbance induced by the combustion process affecting the flow at the inlet. The understanding of such a flow structure is vital for the improvement of the design of high-speed engines as well as the development of flow control methodologies. The characteristics of a shock train at Mach number of 2 in a rectangular channel have been investigated using the 2D RANS equations closed by the Wilcox $k-\omega$ turbulence model.

The sensitivity analysis to grid resolution has demonstrated the high dependence of these kind of flows to the mesh resolution. The difficulties in achieving grid-independent results reflects the characteristic of supersonic flows in long ducts being extremely complicated. The ratio of the thickness of the boundary layer to the channel height has demonstrated to be the key parameter in determining the shock train properties. The shock train establishment in the channel is caused by the interaction with the boundary layer and occurs after a determined length in the channel. A small error in resolving the boundary layer drastically changes the shape of the leading shock, which influences the subsequent portion of the shock train.

Under a sinusoidal forcing, the shock train executes a motion around its mean position that deviates from a perfect sinusoidal profile with variation in oscillation amplitude, frequency, and whether the pressure is first increased or decreased. The shock train demonstrated to have the intrinsic property to be influenced more by a pressure increase rather

than a pressure drop, independent of the back-pressure forcing. To an increase in the back-pressure the shock train responds moving upstream towards the inlet of the computational domain, whereas a decrease in the back-pressure forces the shock train to move towards the outlet. The distance propagated depends on the amplitude of pressure change and is exacerbated with decreasing grid size.

The need to use a two-dimensional code was driven by the setup of the validation case. Although the experimental flow physics is three-dimensional due to the effect of sidewalls, at the centre of the duct the flow can be assumed two-dimensional. The effect of the sidewalls would not change the structure of the shock train since numerical schlieren has successfully replicated the flow field observed with schlieren photography in the reference case. Taking into account the limitation, two-dimensional simulation is a useful tool for the qualitative understanding of the mechanism of formation of the shock train in long ducts. This work has provided the basis to perform a more accurate and realistic investigation of the three-dimensional flow physics in a duct of square cross-sectional area.

-
- ¹ Gnani, F., Zare-Behtash, H., Kontis, K., *Pseudo-shock waves and their interactions in high-speed intakes*, Progress in Aerospace Sciences, **82**:36-56, 2016.
 - ² Su, W.Y., Zhang, K.Y., *Back-Pressure Effects on the Hypersonic Inlet-Isolator Pseudo Shock Motions*, Journal of Propulsion and Power, **29(6)**:1391-1399, 2013.
 - ³ Huang, W., Wang, Z., Pourkashanian, M., Ma, L., Ingham, D.B., Luo, S., Lei, J., Liu, L., *Numerical investigation on the shock wave transition in a three-dimensional scramjet isolator*, Acta Astronautica, **68(11-12)**:1669-1675, 2011.
 - ⁴ Sridhar, T., Chandrabose, G., Thanigaarasu, S., *Numerical Investigation of Geometrical Influence On Isolator Performance*, International Journal on Theoretical and Applied Research in Mechanical Engineering, **2**:7-12, 2013.
 - ⁵ Tian, Y., Yang, S., Le, J., *Numerical study on effect of air throttling on combustion mode formation and transition in a dual-mode scramjet combustor*, Aerospace Science and Technology, **52**:173-180, 2016.
 - ⁶ Klomparens, R., Driscoll, J.F., Gamba, M., *Response of a shock train to downstream back pressure forcing*, AIAA paper, **2016-0078**, 2016.
 - ⁷ Xing, F., Ruan, C., Huang, Y., Fang, X., Yao, Y., *Numerical investigation on shock train control and applications in a scramjet engine*, Aerospace Science and Technology, **60**:162-171, 2017.
 - ⁸ Morgan, B., Duraisamy, K., Lele, S.K., *Large-Eddy Simulations of a Normal Shock Train in a Constant-Area Isolator*, AIAA Journal, **52(3)**:539-558, 2014.
 - ⁹ Weiss, A., Grzona, A., Olivier, H., *Behavior of shock trains in a diverging duct*, Experiments in Fluids, **49(2)**:355-365, 2010.
 - ¹⁰ Babinsky, H., Harvey, J.K., *Shock Wave-Boundary-Layer Interactions*, Cambridge University Press, Cambridge, 2011.
 - ¹¹ Matsuo, K., Miyazato, Y., Kim, H.D., *Shock train and pseudo-shock phenomena in internal gas flows*, Progress in Aerospace Sciences, **35**:33-100, 1999.
 - ¹² Ikui, T., Matsuo, K., *Researches of supersonic flow with the shock wave as main subject*, Japan Society of Mechanical Engineers, **72(609)**:1306-1312, 1969.
 - ¹³ Gawehn, T., Gülhan, A., Al-Hasan, N.S., Schnerr, G.H., *Study on Shock Wave and Turbulent Boundary Layer Interactions in a Square Duct at Mach 2 and 4*, Shock Waves, **20**:297-306, 2010.
 - ¹⁴ Om, D., Childs, M.E., *Multiple Transonic Shock-Wave/Turbulent Boundary-Layer Interactions in a*

- Circular Duct*, AIAA Journal, **23(10)**: 1506-1511, 1985.
- ¹⁵ Heiser, W.H., Pratt, D.T., *Hypersonic airbreathing propulsion*, American Institute of Aeronautics and Astronautics, Washington, D.C., 1994.
 - ¹⁶ Qin, B., Chang, J., Jiao, X., Bao, W., Yu, D., *Numerical investigation of the impact of asymmetric fuel injection on shock train characteristics*, Acta Astronautica, **105(1)**:66-74, 2014.
 - ¹⁷ Wang, C., Xue, L., Tian, X., *Experimental characteristics of oblique shock train upstream propagation*, Chinese Journal of Aeronautics, **30(2)**: 663-676, 2017.
 - ¹⁸ Barber, T.J., Cox, G.B., *Hypersonic vehicle propulsion - A computational fluid dynamics application case study*, Journal of Propulsion and Power, **5(4)**:492-501, 1989.
 - ¹⁹ Mousavi, S.M., Roohi, E., *Three dimensional investigation of the shock train structure in a convergent-divergent nozzle*, Acta Astronautica, **105(1)**:117-127, 2014.
 - ²⁰ Saha, S., Chakraborty, D., *Hypersonic intake starting characteristics - A CFD validation study*, Defence Science Journal, **62(3)**:147-152, 2012.
 - ²¹ Zhang, C., Chang, J., Liu, M., Feng, S., Shi, W., Bao, W., *Effect of heat release on movement characteristics of shock train in an isolator*, Acta Astronautica, **133**:185-194, 2017.
 - ²² Sun, L.Q., Sugiyama, H., Mizobata, K., Fukuda, K., *Numerical and Experimental Investigations on the Mach 2 Pseudo-Shock Wave in a Square Duct*, Journal of Visualization, **6(4)**:363-370, 2003.
 - ²³ Wilcox, D.C., *More advanced applications of the multiscale model for turbulent flows*, AIAA paper 88-220, 1988.
 - ²⁴ Liou, M.S., Adamson Jr, T.C., *Interaction between a normal shock wave and a turbulent boundary layer at high transonic speeds. Part II: Wall shear stress*, Zeitschrift für angewandte Mathematik und Physik, **31(2)**:227-246, 1980.
 - ²⁵ Knight, D.D., *Calculation of Three-Dimensional Shock/Turbulent Boundary-Layer Interaction Generated by Sharp Fin*, AIAA Journal, **23(12)**:1885-1891, 1985.
 - ²⁶ Carroll, B.F., Lopez-Fernandez, P.A., Dutton, J.C., *Computations and experiments for a multiple normal shock/boundary-layer interaction*, Journal of Propulsion and Power, **9(3)**:405-411, 1993.
 - ²⁷ Wilcox, D.C., *Turbulence Modeling for CFD*, DCW Industries, Inc., La Canada, California, 1998.
 - ²⁸ Om, D., Childs, M.E., Viegas, J.R., *Transonic Shock-Wave/Turbulent Boundary-Layer Interactions in a Circular Duct*, AIAA Journal, **23(5)**:707-714, 1985.
 - ²⁹ Chan, W.Y.K., Jacobs, P.A., Mee, D.J., *Suitability of the $k-\varepsilon$ turbulence model for scramjet flowfield simulations*, International Journal for Numerical Methods in Fluids, **70(4)**:493-514, 2012.

- ³⁰ Sun, L. Sugiyama, H., Mizobata, K., Minato, R., Tojo, A., *Numerical and experimental investigations on Mach 2 and 4 pseudo-shock waves in a square duct*, Transactions of the Japan Society for Aeronautical and Space Sciences, **47(156)**:124-130, 2004.
- ³¹ CD-Adapco STAR-CCM+ documentation, 2015.
- ³² White, F.M., *Viscous Fluid Flow*, McGraw-Hill, New York, 2005.
- ³³ Oh, J.Y., Ma, F., Hsieh, S.Y., Yang, V., *Interactions Between Shock and Acoustic Waves in a Supersonic Inlet Diffuser*, Journal of Propulsion and Power, **21(3)**:486-495, 2005.
- ³⁴ Xiong, B., Fan, X.Q., Wang, Y., Zhou, L., Tao, Y., *Back-pressure effects on unsteadiness of separation shock in a rectangular duct at Mach 3*, Acta Astronautica, **141**:248-254, 2017.
- ³⁵ Yamane, R., Kondo, E., Tomita, Y., Sakae, N., *Vibration of pseudo-shock in straight duct, 1st Report, Fluctuation of static pressure*, Bulletin of the JSME, **27(229)**:1385-1392, 1984.
- ³⁶ Yamane, R., Takahashi, M., Saito, H., *Vibration of pseudo-shock in straight duct, 2nd Report, Correlation of static pressure fluctuation*, Bulletin of the JSME **27(229)**:1393-1398, 1984.
- ³⁷ Robinet, J.C., Casalis, G., *Shock Oscillations in Diffuser Modeled by a Selective Noise Amplification*, AIAA Journal **37(4)**:453-459, 1999.
- ³⁸ Wang, S., Ingham, D.B., Ma, L., Pourkashanian, M., Tao, Z., *Turbulence modeling of deep dynamic stall at relatively low Reynolds number*, Journal of Fluids and Structures, **33**:191-209, 2012.
- ³⁹ Smirnov, N.N., Betelin V.B., Nikitin, V.F., Stamov, L.I., Altoukhov, D.I., *Accumulation of Errors in Numerical Simulations of Chemically Reacting Gas Dynamics*, Acta Astronautica, **117**:338-355, 20157.
- ⁴⁰ Hsieh, T., Wardlaw, A. B., Coakley, T., *Ramjet diffuser flowfield response to large-amplitude combustor pressure oscillations*, Journal of Propulsion and Power, **3(5)**:472-477, 1987.
- ⁴¹ Xu, K., Chang, J., Zhou, W., Yu, D., *Mechanism of shock train rapid motion induced by variation of attack angle*, Acta Astronautica, **124**:18-26, 2017.
- ⁴² Culick, F.E.C., Rogers, T., *The Response of Normal Shocks in Diffusers*, AIAA Journal, **21(1)**:1382-1390, 1983.